International Journal of Multiphase Flow 194 (2026) 105443

Contents lists available at ScienceDirect

International Journal of Multiphase Flow

journal homepage: www.elsevier.com/locate/ijmulflow

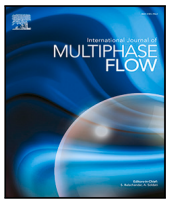

Research Paper

Direct particle–fluid simulation of spherical and ellipsoidal particles in turbulent pipe-free-jet flow

Thede Kiwitt *, Matthias Meinke, Dominik Krug, Wolfgang Schröder

Chair of Fluid Mechanics and Institute of Aerodynamics, RWTH Aachen University, Wüllnerstr. 5a, 52062 Aachen, Germany

ARTICLE INFO

Keywords:
Particle–laden turbulent free jet
Direct particle–fluid simulation
Spherical and ellipsoidal particles

ABSTRACT

The dynamics of spherical and ellipsoidal particles in coupled turbulent pipe-free-jet flow at Reynolds number $Re_D = 15\,546$ is analyzed by direct particle–fluid simulation. The jet is laden with spherical and ellipsoidal particles with aspect ratios in the range $1 \leq \beta \leq 8$ with a volume loading of 6.67×10^{-4} supplied by turbulent periodic pipe flow. The flow field is predicted using a finite-volume formulation on an adaptively refined Cartesian mesh. Each particle is fully resolved by a cut-cell method. The method guarantees the conservation of mass, momentum, and energy at the fluid–particle interfaces. To ensure physically correct particle distributions and flow field characteristics, a slicing technique is used to determine the instantaneous solution of a simultaneously computed particle–laden fully-developed turbulent pipe flow that defines the inflow boundary distribution of the jet. The fluid and particle statistics within fully-developed turbulent pipe and free jet flow are investigated independent from each other. Preferential particle distributions, orientations, and time-averaged energy exchange rates are analyzed with emphasis on the impact of the varying particle aspect ratios. The ellipsoidal particles tend to align closer to the particle center than spherical particles in the turbulent pipe. Furthermore, the energy exchange rates and the particle-induced dissipation tend to differ such that the anisotropic particles exchange more energy with the fluid close to the pipe wall. The impact of the particles on the pipe flow influences the turbulent free jet flow for which it serves as inflow condition. Overall, the spreading rate of the particle–laden turbulent free jet is reduced due to the increased fluid dissipation rate. Furthermore, due to the non-spherical particles the kinetic energy of the fluid is lowered by 9% and the turbulence intensity is decreased by approx. 20% at the end of the near field.

1. Introduction

Flows with solid particles occur in a multitude of natural and technical environments (Hutter, 2005), such as volcano eruptions (Dufek et al., 2012), sandblasting (Kim and Ahn, 2021), industrial combustion chambers (McElroy et al., 1982; Mylläri et al., 2017) etc. In the latter, gaseous fluid transports solid particles which serve as energy carriers that release energy in the combustion process. To mitigate the effects of global warming (Bach, 1981; Martins et al., 2019), fossil fuels are to be replaced by ecological alternatives, e.g., coal is substituted by biomass which can be obtained from sources, such as straw, wheat, tree bark etc. (Tun et al., 2019; McKendry, 2002; García et al., 2017).

Unlike coal particles, however, biomass particles cannot be approximated by spheres since they possess anisotropic shapes. Due to the mostly fibrous structure of the naturally growing resources, the shape of these particles is cylindrical or ellipsoidal rather than spherical (Guo et al., 2012). The behavior of such particles in laminar and turbulent flows differs significantly from that of spherical particles. For instance, the anisotropic shape results in rotational dynamics the impact of which is generally negligible for spherical particles. The rotational dynamics introduces orientation-dependent behavior leading to additional degrees of freedom and interaction phenomena. Hence, the impact of non-spherical particles has to be taken into account to understand the combustion process of biomass particles.

In a first step, the combustion influence is neglected. That is, this numerical investigation focuses on analyzing the impact of non-spherical, ellipsoidal particles on the physics, i.e., the spreading rate, the kinetic energy, the dissipation rate etc., of non-heated turbulent free jet flow.

There is a vast amount of literature on particle–laden flows for configurations like channel flow, pipe flow, and free jet flow. Since the current investigation is defined by the impact of non-spherical, ellipsoidal particles, only experimental and numerical studies of such

* Corresponding author.
E-mail address: t.kiwitt@aia.rwth-aachen.de (T. Kiwitt).

https://doi.org/10.1016/j.ijmultiphaseflow.2025.105443
Received 7 April 2025; Received in revised form 25 August 2025; Accepted 2 September 2025
Available online 10 September 2025

non-spherical particle–laden flows are discussed in the following. To the best of the author's knowledge, the number of journal publications in the field of non-spherical isothermal pipe or free jet flows is low. We do include pipe flow in the chronological literature review since the pipe flow determines the inflow distribution of the turbulent free jet.

Black and McQuay (2001) performed experiments in co-axial jet and swirling flows to assess the influence of the shapes of spherical and non-spherical particles on the particle dynamics. The two-component phase-Doppler particle analyzer technique was used to collect data for the particle velocities. The authors observed that non-spherical particles follow the fluid velocity much closer than the spherical particles. The essential reasons for these results are: First, the non-spherical particles show an increase in the drag coefficient which lowers the response time. The drag forces depend on the particle orientation such that the non-spherical particles tend to behave more like the gas phase. Finally, the terminal velocity of the non-spherical particles is lower than that of the spherical particles.

Ljus et al. (2002) experimentally investigated spherical and pulp fiber particles with large aspect ratios in turbulent pipe flow. The Reynolds number based on the bulk velocity was in the range 82 000 – 130 000 and the particle mass loading was 0.01 – 0.1. The measurements were conducted using a wedge-shaped hot-film probe with a static calibration method. The authors reported significant turbulence intensity modulation by the particles. The modulation impact depended on the particle diameter. Whereas spherical particles showed a modulation as a function of the radial position, the pulp fibers were shown to decrease the turbulence intensity over the whole cross sectional area.

Qi et al. (2015) presented experimental measurements of fibrous particles with long aspect ratios in turbulent pipe-jet flow. The bulk velocity Reynolds number was 70 000 and the fiber aspect ratio was 40. Particle-tracking velocimetry was used to measure the particle characteristics. The results showed that the fibers possess a preferential orientation at 54° to the axial direction. However, the orientations covered a wide range spanning 30° – 90°. The absolute value of the mean angular velocity of the fibers increased with the radial distance from the axis centerline such that the lowest angular velocity was observed at the centerline of the jet.

Gupta et al. (2018) numerically investigated the effect of the particle shape of prolate ellipsoids on the fluid statistics in particle–laden turbulent pipe flow at $Re_\tau \approx 250$ and volume loading $\zeta_v = 0.48\%$. The finite-sized particles with aspect ratios in the range $\beta = 1$, $\beta = 2$, and $\beta = 3$ are compared with a single-phase reference solution. It was shown that the local accumulation of particles close to the wall decreases for ellipsoids with increasing aspect ratio due to slower rotation than the spheres near to the wall. The prolate particles tend to align with their major axes in the streamwise direction.

Guo et al. (2019) used a model that accounts for spheroidal particle drag force and torque within an Eulerian-Lagrange model to simulate pulverized biomass jets. The findings of particle and fluid velocities yielded large differences. It was also shown that the spheroid model led to a more dispersed distribution regarding the particle residence time and local concentration compared to the reference models.

The literature review shows that there are hardly any detailed results on non-spherical, ellipsoidal particle–laden turbulent free jets. That is, the impact of the shape of non-spherical, ellipsoidal particles on the orientation and the preferential distribution of the particles, the fluid kinetic energy, the jet geometry etc. are not discussed in the existing literature. These questions will be addressed in this study by performing direct particle–fluid simulations for a non-spherical particle–laden turbulent free jet and comparing the multiphase jet flow data with single-phase turbulent free jet data for the same flow parameters. The direct comparison highlights the modulation impact of the particles. Energy and turbulence statistics are shown and the impact of the spherical and ellipsoidal particle characteristics are discussed.

This manuscript is structured as follows. First, the governing equations for the fluid and the particle phase will be presented in Section 2. In Section 3, the numerical setup will be described and the flow and particle parameters will be discussed in Section 4. The validation of the numerical results will be presented in Section 5. The results of the direct particle–fluid simulation are analyzed in Section 6, followed by a brief conclusion in Section 7.

2. Governing equations

2.1. Fluid flow

The flow of a compressible, viscous fluid is described by the Navier–Stokes equations. The equations of conservation of mass, momentum, and energy read

$$\frac{d}{dt}\int_V \rho dV + \oint_{\delta V} [\rho \mathbf{u}] \cdot \mathbf{n} dA = 0 \tag{1a}$$

$$\frac{d}{dt}\int_V \rho \mathbf{u} dV + \oint_{\delta V} [\rho \mathbf{u}\mathbf{u} + \underline{\sigma}] \cdot \mathbf{n} dA = \mathbf{0} \tag{1b}$$

$$\frac{d}{dt}\int_V \rho E dV + \oint_{\delta V} [\rho E \mathbf{u} + \underline{\sigma} \cdot \mathbf{u} + \mathbf{q}] \cdot \mathbf{n} dA = 0\,, \tag{1c}$$

where ρ denotes the density, $\mathbf{u}$ the velocity vector with the components u, v, and w in x, y, and z direction, $\underline{\sigma}$ the stress-tensor, δV the control volume surface with the outward-facing normal $\mathbf{n}$, E the total energy, and $\mathbf{q}$ the vector of heat conduction.

The stress-tensor $\underline{\sigma}$ is described by

$$\underline{\sigma} = -2\mu \underline{\mathbf{S}} + \frac{2}{3}\mu(\nabla \cdot u)\underline{\mathbf{I}} + p\underline{\mathbf{I}}, \tag{2}$$

with the dynamic viscosity μ, the unit tensor $\underline{\mathbf{I}}$, the fluid pressure p, and the rate-of-strain tensor $\underline{\mathbf{S}} = \frac{1}{2}[\nabla \mathbf{u} + (\nabla \mathbf{u})^T]$ for a Newtonian fluid of vanishing bulk viscosity.

The Fourier law is

$$\mathbf{q} = -k(T)\nabla T, \tag{3}$$

with the thermal conductivity

$$k(T) = T^{3/2}\left(\frac{1 + S_k}{T + S_k}\right), \tag{4}$$

where S_k is the thermal Sutherland constant. T is the temperature computed by the equation of state for a perfect gas $T = \gamma\ p/\rho$ where the heat capacity ratio $\gamma = 1.4$ is used to determine the heat conduction $\mathbf{q}$ (White, 2006).

The dynamic viscosity μ is determined by Sutherland's law

$$\mu(T) = T^{3/2}\left(\frac{1 + S_\mu}{T + S_\mu}\right), \tag{5}$$

with the Sutherland constant S_μ.

The Reynolds number

$$Re_D = \frac{\rho_j u_b D}{\mu_j} \tag{6}$$

is determined by the bulk velocity u_b, the pipe diameter D, and the density and dynamic viscosity in the inflow cross section denoted by the subscript $(\cdot)_j$.

The friction Reynolds number

$$Re_\tau = \frac{u_\tau D}{\nu} \tag{7}$$

is based on the friction velocity $u_\tau = \sqrt{\frac{\tau_w}{\rho}}$ with the wall-shear stress in the pipe $\tau_w = \mu \frac{\partial u}{\partial y}|_{r=R}$.

The Prandtl number

$$Pr = \frac{c_p \mu_j}{k_j} \tag{8}$$

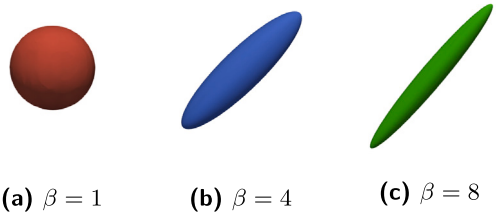

Fig. 1. Spherical and ellipsoidal particles for aspect ratios $\beta = 1$, $\beta = 4$, and $\beta = 8$.

is determined by the viscosity and thermal conductivity at the jet inflow section and the specific heat at constant pressure.

The particle Stokes number based on the time scale $\tau_0 = D/u$ of the turbulent flow in the exit cross section of the pipe at $x/D = 0$ is

$$St_0 = \frac{Re}{18} \cdot \frac{\rho_p}{\rho_f} \cdot \left(\frac{d_{eq}}{D}\right)^2 \tag{9}$$

as commonly used in the analysis of interaction between particle and free jet flow (Lau and Nathan, 2014). The quantity d_{eq} is the volume-equivalent particle diameter and $\frac{\rho_p}{\rho_f}$ is the ratio of particle and fluid densities.

2.2. Particles geometry and motion

The particles are characterized by the aspect ratio

$$\beta = \frac{c}{a} \tag{10}$$

with the condition

$$\frac{x^2}{a^2} + \frac{y^2}{b^2} + \frac{z^2}{c^2} = 1. \tag{11}$$

The quantities a, b, and c are half the length of the principal axes. Spherical particles are defined by $\beta = 1$. For the prolate particles, the two minor axes are equal, i.e., $a = b$, and $c > a$ resulting in $\beta > 1$. The investigated particles are exemplarily shown in Fig. 1.

To ensure that all particles, irrespective of their aspect ratio, have the same mass, the individual axis lengths are scaled such that all particles have the same volume, i.e., $V_{eq} = \frac{4\pi}{3} a\,b\,c = \frac{4\pi}{3}\left(\frac{d_{eq}}{2}\right)^3$ and the same particle density.

The movement of the particles is determined by the mechanical loads on the particles resulting in translational and rotational motion.

Linear acceleration $\frac{d\mathbf{u}_p}{dt}$ of particle $(\cdot)_p$ is modeled by Newtons second law of motion

$$m_p \frac{d\mathbf{u}_p}{dt} = \mathbf{F}_p, \tag{12}$$

with the particle mass m_p and the integrated force at the surface $\mathbf{F}_p$ of the particle.

The rotational motion is described by

$$\hat{\boldsymbol{\mathcal{I}}} \frac{d\hat{\boldsymbol{\omega}}_p}{dt} + \hat{\boldsymbol{\omega}}_p \times \left(\hat{\boldsymbol{\mathcal{I}}} \hat{\boldsymbol{\omega}}_p\right) = \hat{\boldsymbol{\mathcal{T}}}_p, \tag{13}$$

with the diagonal tensor containing the principal moments of inertia $\boldsymbol{\mathcal{I}}$ and the angular velocity $\boldsymbol{\omega}_p$ which are defined with respect to the particle-fixed frame of reference $\hat{(\cdot)}$.

The resulting forces

$$\mathbf{F}_p = \oint_{\Gamma_p} (-p\mathbf{n} + \underline{\tau} \cdot \mathbf{n})\, dA \tag{14}$$

are reduced to the particle center of mass by integrating the individual pressure and shear-stress forces acting on the surfaces of the bodies.

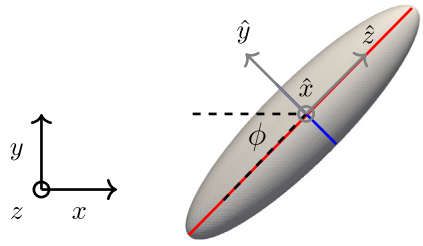

Fig. 2. Global coordinate system (x, y, z), particle fixed coordinate system $(\hat{x}, \hat{y}, \hat{z})$, and inclination angle ϕ. The aspect ratio β is the ratio of the major axis c in red and the minor axis a in blue. The angle ϕ is in relation to the streamwise flow direction.

The resulting torque with respect to the center of mass of the bodies reads

$$\boldsymbol{\mathcal{T}}_p = \oint_{\Gamma_p} (\mathbf{x_p} - \mathbf{x}_{\Gamma_p}) \times (-p\mathbf{n} + \underline{\tau} \cdot \mathbf{n})\, dA, \tag{15}$$

with the distance of the surfaces to the particle center $\mathbf{x} - \mathbf{x_p}$.

The multiphase system is described by two distinct coordinate systems. The global coordinate system (x, y, z) is fixed at the center of the fluid domain whereas the particle coordinate system $(\hat{x}, \hat{y}, \hat{z})$ is fixed at the center of mass of each particle. The relative rotation between the two coordinate systems is expressed by a quaternion-based notation as shown in Fig. 2. More details are described in Siewert et al. (2014).

Buoyancy and gravitational forces are intentionally neglected to focus on the interaction between the particles of varying shapes and the carrier fluid. This approach simplifies the quantification of forces, allowing for an assessment of isolated interactions.

2.3. Phase interface exchange

The full resolution of the flow field over the particles allows the determination of all interaction forces between the carrier fluid and the particles. The rate of kinetic energy ψ transferred from the number of N_p particles to the surrounding fluid is determined by the net force $\boldsymbol{F}_p$ and torque $\boldsymbol{\mathcal{T}}_p$ acting on the particle surface.

With the acting surface forces $\mathbf{F}_p$ and the torque $\mathcal{T}_p$ exerted on the particle and under consideration of the identity $(\mathbf{a} \times \mathbf{b}) \cdot c = (\mathbf{b} \times \mathbf{c}) \cdot a$, the direct transfer of kinetic energy via linear and angular momentum is given by

$$\psi(t) = \sum_{p=1}^{N_p} \psi_p = -\sum_{p=1}^{N_p} (\mathbf{F_p} \cdot \mathbf{u_p} + \boldsymbol{\mathcal{T}}_\mathbf{p} \cdot \boldsymbol{\omega}_p). \tag{16}$$

While $\psi(t)$ quantifies the direct transfer of kinetic energy from one phase to the other, the particles additionally influence the fluid energy by modulating the dissipation rate $\epsilon(t)$

$$\epsilon(t) = \int_{V_f} \left[\underline{\tau} : (\nabla \mathbf{u}) - (\nabla \cdot \mathbf{u})\, p\right] dV \tag{17}$$

in the fluid control volume V_f. The control volume $V_f = \sum_p \backslash \Gamma_p$ with the volume surrounding the particle $\sum_p$ and the particle volume Γ_p encapsulates the particles and the fluid within a certain volume of the particle surfaces. The volume of V_f is chosen such that it is not significantly larger than the local characteristic length scale of the flow. It is smaller than 4 d_{eq} where a distance-based weighting is used, and is attached to the moving surface of the particle. The particle-induced dissipation rate is derived from the conservation laws, i.e., the momentum equation is considered. Multiplication of the momentum equation with the particle velocity $\mathbf{u}$, consideration of the identity $\nabla \cdot (\tau \cdot \mathbf{u}) = \mathbf{u}(\nabla \cdot \tau) + \tau : (\nabla \mathbf{u})$, and formulation in a non-inertial frame of reference yields the dissipation rate ϵ due to internal friction and compressibility effects of pressure dilatation within the control volume.

For a detailed description and validation of the interface energy exchange dynamics and the particle-induced dissipation rate, the reader is referred to Schneiders et al. (2017).

The decay rate of fluid kinetic energy $E_k = \int_{V_f} \frac{1}{2}\rho \mathbf{u}^2 dV$ with embedded rigid particles is computed by

$$\frac{dE_k}{dt} = \psi(t) - \epsilon(t), \tag{18}$$

which allows the analysis of the temporal development of the fluid kinetic energy and the interphase energy exchange (Schneiders et al., 2019).

3. Numerical method

3.1. Fluid phase

The governing equations for the carrier fluid Eq. (1) are solved by a finite-volume solver using a cut-cell method formulated for a solution-adaptive hierarchical Cartesian grid (Hartmann et al., 2008).

The viscous fluxes are determined by a central scheme, whereas the inviscid fluxes are computed by an upwind-biased scheme. The equations are integrated in time by a five-stage predictor–corrector Runge–Kutta scheme (Schneiders et al., 2013, 2016).

A multi cut-cell method is utilized for the discretization of the particle surfaces which are tracked using a signed-distance multi level-set function $\xi(\mathbf{x}, t)$ (Schneiders et al., 2013; Günther et al., 2014). The cut-cell method reshapes the Cartesian cells intersected by the surfaces of the particles. If necessary, multiple cuts of a single cell are performed by adding cut surfaces accordingly. Thus, particle–particle or particle–wall interactions can occur on a sub-cell length level.

3.2. Particle phase

The linear particle dynamics are determined by solving the equations defining the translational motion of the particles Eq. (12), which is advanced in time by an implicit Newmark scheme. The integration of the equation governing the rotational dynamics, Eq. (15), is performed using a Crank–Nicolson scheme.

Particle–particle and particle–wall collisions are modeled using a modified version of the collision model proposed by Glowinski et al. (2001). Due to the anisotropic shape of some of the particles and the curvature of the pipe walls, the collision model is extended to operate on generic non-spherical body shapes. It additionally includes the point-of-attack in relation to the center of mass such that the rotational momentum is correctly applied. The collisions of fully-resolved arbitrary shaped solid bodies $(\cdot)_p$ and $(\cdot)_q$ are computed for the contact point which is equivalent to the nearest surfaces of the bodies. No collision is considered if $(\mathbf{x_p} - \mathbf{x_q}) - (r_{max,p} + r_{max,q}) > S$, where the quantities x_p, x_q and $r_{max,p}$, $r_{max,q}$ are the center of mass of the particles and the maximum radius of the non-spherical, ellipsoidal particles and S defines a minimum gap between the particles. The maximum radius $r_{max,i}$ is defined by the major axis c_i of the particles such that a numerically efficient prediction for the collision is feasible. The parallel alignment of the major axis $c_i = r_{max,i}$ indicates the configuration with the minimum distance between the particles, i.e., the case where a collision is most likely to occur. If a collision occurs, the repulsive force

$$f_{p,i} = C_0 \cdot \left(\frac{S - l_d}{S}\right)^2 \cdot \frac{x_{p,i} - x_{q,i}}{l_d} \tag{19}$$

with

$$C_0 = f_r \cdot \frac{\frac{1}{2} \cdot (m_p + m_q) \cdot u_b^2}{l_{max}} \tag{20}$$

is calculated by the repulsive force factor f_r, the particle masses m_p and m_q, the bulk velocity u_b, the cell length of an uncut cell l_{max} at the max level, the distance between the surfaces l_d, and the distance between the center of mass $x_{p,i} - x_{q,i}$ in the direction i of the body $(\cdot)_p$. Collisions are assumed to be fully elastic and the loss of kinetic energy due to collisions and particle deposition at the wall is not considered.

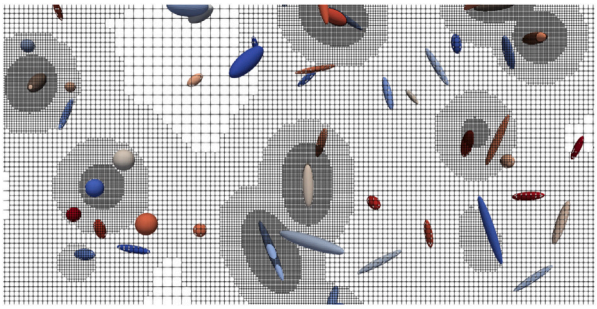

Fig. 3. Snapshot of the Cartesian mesh in the particle–laden pipe flow domain. The grid is locally refined according to flow sensors and the particle surface locations. Note that for better visibility a $2D$ mesh is shown. Particles out of the mesh plane are shown colored by their respective particle id.

The mesh is locally refined based on distinct flow field characteristics, i.e., the refinement is controlled by data based on the velocity derivatives and the vorticity of the instantaneous flow field. Moreover, the volume surrounding the particles and the pipe walls is refined to the highest predefined mesh refinement level. This approach ensures a sufficiently accurate resolution around all solid surfaces. Simultaneously, the total amount of mesh points is minimized such that the computational cost are significantly reduced. The mesh around a number of particles is illustrated in Fig. 3.

The combined number of grid cells in the pipe and the free jet domains is in the range of 1.3 billion cells. Typically, the pipe domain contains approx. 15% of all cells which results in an average of approx. 200 million cells for the pipe and 1 100 million cells for the turbulent free jet domain. The time step $\Delta t u_b / D \approx 0.00005$ is determined by the stability condition of the numerical scheme and the resolution at the wall is $\Delta y^+ \approx 1.22$. The particle resolution is $d_{eq}/\Delta_{min} = 14$ such that the volume-equivalent diameter is covered by 14 grid cells.

Due to the large number of mesh cells, the simulations are executed on a high-performance computing system. To achieve a high parallel efficiency, dynamic load-balancing is used to redistribute the varying workload due to the solution adaptive mesh and the moving particles (Niemöller et al., 2020; Wegmann et al., 2025).

3.3. Domain of integration

A schematic of the pipe and the free jet domain is shown in Fig. 4. Both domains possess their own mesh resolution. However, the mesh in the crossflow section of the pipe is identical to that at the inflow boundary of the jet domain such that the solution in the pipe domain can be transferred at each time step without interpolation. The particles with all information are transferred accordingly. The slicing technique guarantees physically correct velocity distributions, particle positions and particle velocities as inflow conditions for the jet domain such that no assumptions regarding the turbulent flow state or particle dynamics have to be made (Burattini et al., 2004).

The fully-developed turbulent pipe flow is simulated by a periodic boundary condition in the streamwise direction, where a volume forcing is applied to mimic a pressure gradient in the axial direction. While the free jet is coupled to the solution in the pipe flow, the solution in the pipe domain is independent from the solution in the free jet domain, i.e., one-directional coupling is applied.

The pipe has a diameter D and a length $L/D = 6$. This streamwise extent is based on the work of Chin et al. (2010) in which the influence of the periodic pipe length on the turbulence statistics was investigated. The free jet domain consists of a box with a length of $50D$ in the

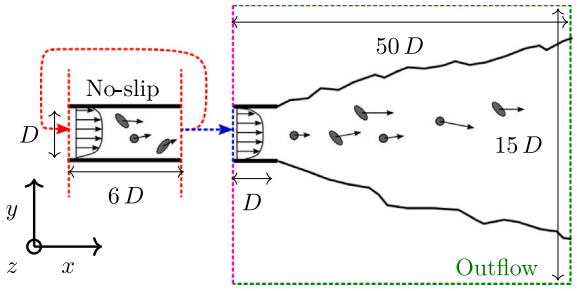

Fig. 4. Schematic illustration of the slicing technique to determine the inflow condition for the particle–laden jet. The simulations for the pipe and jet domains are conducted concurrently. A plane of the fully-developed pipe flow solution is transferred to the inflow boundary of the jet domain at each time step. The sketch also defines the domain sizes and imposed boundary conditions: periodic boundary conditions are implemented at the pipe in- and outlet, while outflow boundary conditions are defined on all other boundaries of the jet domain outside of the pipe. A no-slip isothermal wall boundary condition is used on the pipe wall.

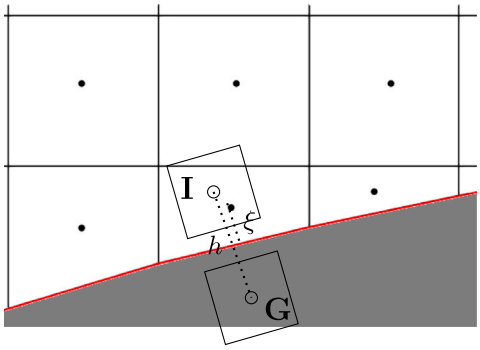

Fig. 5. Schematic of the prescription of ghost cells. Ghost cell values G are determined at a mirror position of a reconstructed image point I at a distance h. A multiple ghost cell approach is used for the simulation.

streamwise and $15D$ in the radial direction. Note that the pipe domain extends a length of one D into the jet domain as sketched in Fig. 4. There is no coflow around the free jet.

3.4. Boundary conditions

On the outflow boundaries of the free jet domain the static pressure is prescribed. Neumann type boundary conditions are defined for the density and velocity. When particles enter or exit the domain, a special treatment around the particles is applied that is discussed in Section 3.6.

The boundary conditions on the particle surfaces are formulated using ghost cells as sketched in Fig. 5. The ghost cell values G are determined at the mirror position

$$\mathbf{x}_G = \mathbf{x}_C - max\left(\ 2\xi,\ \xi + \frac{h}{2}\right) \cdot \mathbf{n}_\Gamma \tag{21}$$

normal to an image point I.

The velocity in the ghost cell $\mathbf{u_G}$ is prescribed using a Dirichlet type boundary condition, i.e.,

$$\mathbf{u_G}(\mathbf{x}, t) = 2\mathbf{u}_\Gamma(\mathbf{x}, t) - \mathbf{u_I}(\mathbf{x}, t)\ , \tag{22}$$

where $\mathbf{u}_\Gamma(\mathbf{x}, t)$ denotes the surface velocity and $\mathbf{u_I}(\mathbf{x}, t)$ the velocity at the image point which is determined using a least-squares interpolation in the direction normal to the ghost cell surface.

For the pressure p_G in the ghost cells, Robin boundary conditions

$$\frac{p_C - p_G}{\xi + h/2} + \kappa \frac{\xi\ p_G + h/2\ p_C}{\xi + h/2} = 0 \tag{23}$$

based on the cell pressure p_C, the distance between the ghost cell and the inner cell h, the cell surface distance ξ, and the material derivative $D\mathbf{u}/Dt$ and $\kappa = \gamma T_\Gamma^{-1}\ (D\mathbf{u}/Dt \cdot\ \mathbf{n})_\Gamma$ are prescribed. The density ρ_G is determined analogously. See Schneiders et al. (2016) for more details.

Similar boundary conditions are imposed on the pipe wall. However, these are formulated for a non-moving surface, i.e., the ghost cell velocity $\mathbf{u_G}$ is set to

$$\mathbf{u_G}(\mathbf{x}, t) = -\mathbf{u_I}(\mathbf{x}, t) \tag{24}$$

such that the velocity at the surface Γ is zero. The pipe wall temperature is set constant.

3.5. Slicing technique

The coupling of the fully-developed turbulent pipe flow and the free jet flow is conducted by a slicing technique. In the simulation framework m-AIA (multiphysics-Aerodynamisches Institut Aachen), the full domain consisting of the pipe and free jet domain is modeled by a joint grid approach (Hartmann et al., 2008; Wegmann et al., 2025). The full grid is consequently adapted such that the pipe domain and the free jet domain are independent subdomains. However, the pipe end domain and the jet inflow domain overlap. The adaptive mesh is kept consistent in the overlapping area such that the information from the pipe to the free jet domain can be directly transferred. Hence, the particles are transferred equally by using threshold boundaries inside the pipe domain. Upon crossing the threshold, particles are transferred to the free jet inflow section with all relevant particle data such as, e.g., particle velocity, orientation etc. This approach ensures a smooth transition of the particles and the fluid since the threshold boundaries are placed such that a gradual entering of the spherical ellipsoidal particles in the free jet domain is given.

3.6. Description of particle surfaces

The particle surfaces are tracked using analytical signed-distance or level set functions $\xi(\mathbf{x}, t)$, which are evaluated for the mesh cells at each time step if necessary. These values, which are related to the center of the Cartesian cells, are used to compute the intersections of the particles with the cell surfaces and to identify the mesh cells which should be refined around the moving particles.

Unlike in the streamwise periodic pipe flow simulation, special consideration must be taken for entering and exiting particles in the free jet simulation to ensure that the intersections of the particles with the cells are determined consistently. In the current cut-cell formulation, the cut surfaces are computed from level-set values interpolated at the nodal points from neighboring cell centers. This requires the cell centered level-set values around the nodes. Therefore, additional cells located outside the domain are required at the boundaries to compute the correct nodal level-set values. These cells are added dynamically during runtime of the simulation to allow particles to cross the jet domain boundaries without generating artificial perturbations. Fig. 6 shows a sample configuration to highlight the difference in the surface representation with and without the additional cells. Without the additional cells, the intersections are not determined consistently, which has a negative effect on the stability of the numerical method and the conservation properties of the used algorithm.

4. Flow and particle parameters

The Reynolds number based on the pipe diameter and the velocity at the jet inflow section is $Re_D = 15\,546$ and the friction velocity Reynolds number is $Re_\tau = 448$. The Mach number is $M = 0.1$ and the Prandtl number is $Pr = 0.72$.

The particles are initially placed at random locations within the pipe domain and the initial particle velocity equals the local fluid velocity. Random orientations of the particles are assumed. The particle aspect

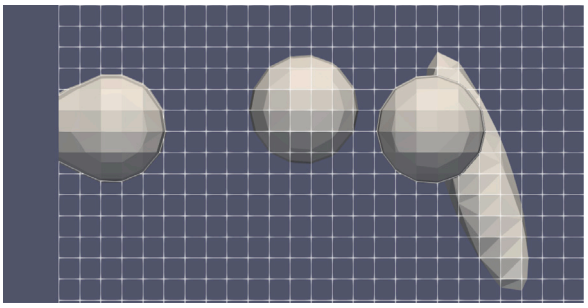

(a) Reconstruction of cut cell surfaces for a particle entering the domain without additional cells outside of the domain.

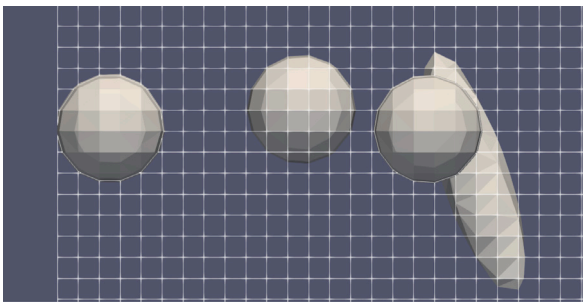

(b) Reconstruction of cut cell surfaces for a particle entering the domain with additional cells outside of the domain. The additional cells are not shown.

Fig. 6. Representation of the cut-cell surfaces without (a) and with (b) additional level-set cells outside of the domain. Without additional cells an incorrect surface representation is obtained, whereas the sharp resolution of the particle cell surface is ensured in the second case. Due to the sharp resolution of the cut-cell surfaces, the conservatism is maintained even for particles crossing boundaries.

Table 1
Particle parameters.

Particle parameter	Value
Diameter d_{eq}/D	0.01
Aspect ratio β	1,2,3,4,5,6,7,8
Percentage of each β	12.5%
Density ratio ρ_p/ρ_f	600
Volume loading ζ_v	0.00667
Mass loading ζ_m	0.4
Stokes number St_0	50

ratios cover the range $1 \leq \beta \leq 8$. The spectrum of the aspect ratio for the particles is uniform, i.e., equal amounts of particles (12.5%) for each of the 8 different aspect ratios are ensured. As stated before, all particles have the same volume based on the volume-equivalent diameter which is $d_{eq}/D = 0.01$. All particles have the same density ratio $\rho_p/\rho_f = 600$ which is relevant for biomass particles (Guo et al., 2012). The particle Stokes number is $St_0 = 50$.

The volume loading in the pipe domain is approx. $\zeta_v = 6.67 \times 10^{-4}$ and the resulting mass loading is $\zeta_m \approx 0.4$. The number of particles in the pipe domain is 5 981. It remains constant due to the periodic boundary conditions for the pipe simulation. In the near field of the jet $x/D \leq 10$, the number of particles fluctuates due to the constant injection of new particles and the exiting of old particles from the free jet domain. It slightly varies since the number of particles entering is not necessarily identical to the number of particles exiting the jet domain. On average, the number of particles in the free jet domain is approx. 10 000 at all time steps.

The particle parameters are summarized in Table 1.

5. Validation

The numerical methods have been extensively validated for single-particle flows in Schneiders et al. (2016) and for particles in isotropic turbulent flows (Schneiders et al., 2017, 2019; Fröhlich et al., 2021).

To validate the numerical method for pipe flow and the turbulent free jet configuration, a single-phase pipe flow and a turbulent free jet are computed. The findings are compared with numerical and experimental data from (Pirozzoli et al., 2021; Chin et al., 2010, 2014; Papadopoulos and Pitts, 1999).

5.1. Fully-developed turbulent pipe flow

The Reynolds number based on the friction velocity is $Re_\tau = 448$ while it is $Re_D = 15\,546$ based on the bulk velocity $\overline{u}_b$ at the jet inflow section. This is somewhat different from the Reynolds number $Re_\tau = 500$ in Chin et al. (2010, 2014) and slightly lower than $Re_\tau \approx 450$ in Pirozzoli et al. (2021). A 118 million-cell mesh was used with local mesh refinement of the viscous wall layer.

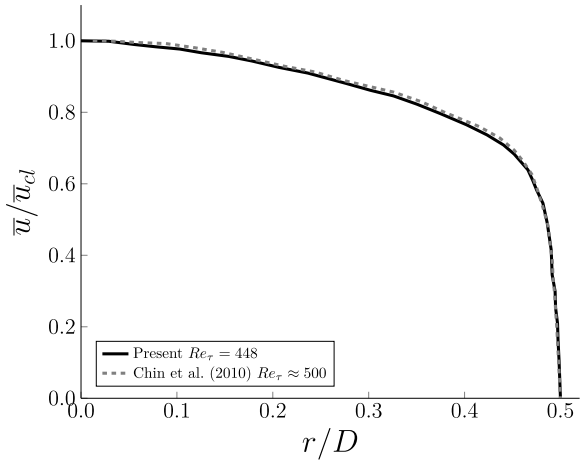

Fig. 7. Time and streamwise averaged velocity component $\overline{u}/\overline{u}_{cl}$ normalized by the maximum velocity on the centerline as a function of the radius r/D. The solution is compared with results of Chin et al. (2010).

The time and streamwise averaged axial velocity profile as a function of the radial direction r normalized by the centerline velocity $\overline{u}_{cl}$ is compared in Fig. 7 with the data of Chin et al. (2010). The results are in close agreement. The maximum discrepancy between the velocity distributions is below 3%. Furthermore, the time-averaged centerline velocity is $\overline{u}_{cl}/u_b = 1.27$ which agrees with the result $\overline{u}_{cl}/u_b = 1.27$ in Pirozzoli et al. (2021).

The distribution of the root-mean-square of the velocity fluctuations normalized by the friction velocity u_τ is shown in Fig. 8. Again, the maximum deviation between the current data and data by Chin et al. (2010) is 3% which is acceptable due to the slightly different friction velocity Reynolds numbers.

It is fair to conclude that the velocity field in the single-phase pipe flow is accurately predicted by the numerical method.

5.2. Turbulent free jet flow

To further validate the numerical approach for a turbulent free jet including the slicing technique, a single-phase jet is simulated. The Reynolds number $Re_D = 15\,546$ is that of the latter discussed particle–laden jet since the single-phase data serve as reference solution for

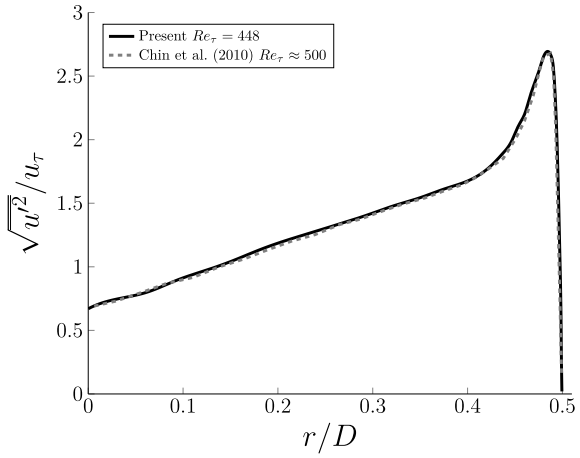

Fig. 8. Streamwise root-mean-square velocity fluctuations normalized by the wall-friction velocity $\sqrt{\overline{u'^2}}/u_\tau$ as a function of the distance from the centerline r/D compared with results from (Chin et al., 2010).

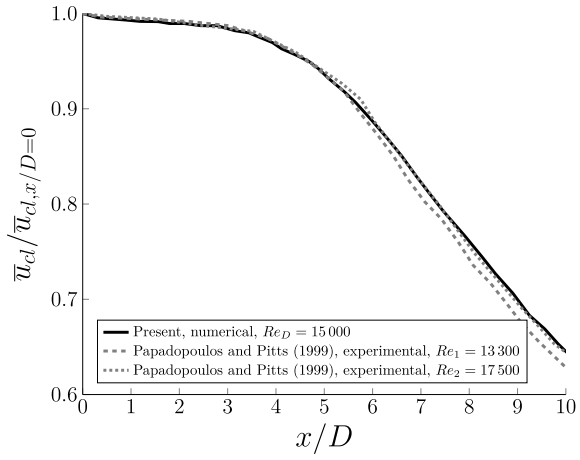

Fig. 9. Centerline velocity normalized by the centerline velocity at the nozzle exit $\overline{u}_{cl}/\overline{u}_{cl,0}$ compared with experimental data from (Papadopoulos and Pitts, 1999).

the multiphase solution. The mesh contains 118 million cells for the periodic pipe domain and 593 million cells for the turbulent free jet. Furthermore, the schematic of the turbulent free jet in Fig. 4 is also valid for the single-phase flow.

The mean velocity profile $\overline{u}_{cl}/\overline{u}_{cl,x=0}$ along the centerline in the axial direction of the free jet domain is compared with experimental data from (Papadopoulos and Pitts, 1999) in Fig. 9. The authors conducted measurements for two jets at Reynolds numbers based on the bulk velocity $Re_1 = 13\,300$ and $Re_2 = 17\,500$. In the experimental setup, the jet emerges from a long straight pipe such that a fully-developed turbulent pipe flow at the exit is ensured. The comparison of the present numerical and the experimental results show good agreement. The deviation at various distances from the nozzle exit is below 4%.

6. Results and discussion

The following section presents the temporally averaged results of the particle–laden turbulent pipe and free jet flow. The temporal average is determined by comparing several time intervals that cover different time spans. The findings do not evidence any substantial differences such that the averaged data are a sound basis for the following discussion. An overall impression of the instantaneous flow field is shown in Fig. 10 in which the distribution of the particles and the development of the potential core, that is defined by the region near the centerline that has almost uniform mean velocity, and the free-shear layers are indicated.

The fully-developed pipe flow determines the instantaneous inflow for the free jet flow. Therefore, the flow dynamics of the fully-developed particle–laden pipe flow is investigated first. The spatial distribution and relative velocity between the particles and the fluid in the pipe flow are discussed and the energy exchange between the solid and fluid phase is analyzed with emphasis on the impact on the fluid dissipation. Subsequently, the results for the turbulent free jet are presented. The influence of the particles on the turbulence characteristics of the carrier fluid in the jet near field $x/D \leq 10$ will be investigated in detail.

6.1. Fully-developed particle–laden turbulent pipe flow

The turbulent flow in the pipe is simulated concurrently with the flow in the jet domain. As stated before, one-way coupling is used such that the pipe flow solution is not influenced by the jet results. The particle dynamics are analyzed statistically and the interaction between the two phases is discussed.

6.1.1. Particle distribution

The dynamics of spherical and non-spherical, ellipsoidal particles differ. Due to their anisotropic shape, ellipsoidal particles show a concentration maximum in a turbulent pipe flow at a radius different from that of spherical particles. The time-averaged particle distribution in the pipe is shown in Fig. 11(a) for spherical and ellipsoidal particles, i.e., for individual aspect ratios and the mean for all aspect ratios $\beta \geq 2$. The same data is plotted scaled by $1/r$ in Fig. 11(b), i.e., scaled by the relative distance to include the impact of the locally varying cross-sectional area in circular pipe geometries.

The general trend of ellipsoidal particles to accumulate closer to the pipe wall rather than in the pipe center is indicated. This tendency denoted as turbophoresis indicates a preferential distribution in the direction of decreasing turbulence, i.e., near the wall in wall-bounded flow. The behavior is well-known for spherical particles and is said to be caused by the drag force at the particle surfaces and the gradient of turbulence intensity within the turbulent flow (Reeks, 1983; Crowe, 2005; Bec and Vallée, 2024).

For non-spherical particles, the present results show an approximately linear increase in concentration with increasing pipe radius until a maximum is reached at $r/D \approx 0.32$. Spherical particles show a maximum concentration closer to the pipe wall at approx. $r/D \approx 0.4$.

The statistical particle concentration is linked to the average residence time of particles at specific radial locations which depends on the local radial velocity of the particles. Consequently, the probability of a particle being located at a certain radius is higher where the radial velocity is smaller such that higher dwell times are observed. In Fig. 12, the radial velocity $u_R = \frac{yv+zw}{\sqrt{y^2+z^2}}$ normalized by u_b for aspect ratios $\beta = 1$, $\beta = 2$, $\beta = 4$, and $\beta = 8$ as a function of the radial coordinate r/D is presented.

The comparison between spherical and ellipsoidal particles reveals that the magnitude of radial velocity varies across different aspect ratios. While all curves exhibit a similar trend of increased velocities at the pipe center and the wall, particles with larger aspect ratios demonstrate higher radial velocities and thus, increased momentum and larger velocity. This increase in radial velocity, particularly noticeable near the pipe center and the pipe wall, results in a lower probability of particle presence in these regions due to reduced residence time.

The particles move away from the pipe center ($u_R > 0$) and the pipe wall ($u_R < 0$). The time-averaged radial velocity of $u_R/u_{bulk} \approx 0$ in the area between the pipe center and the pipe wall indicates longer dwell times of the particles which results in the probability density function

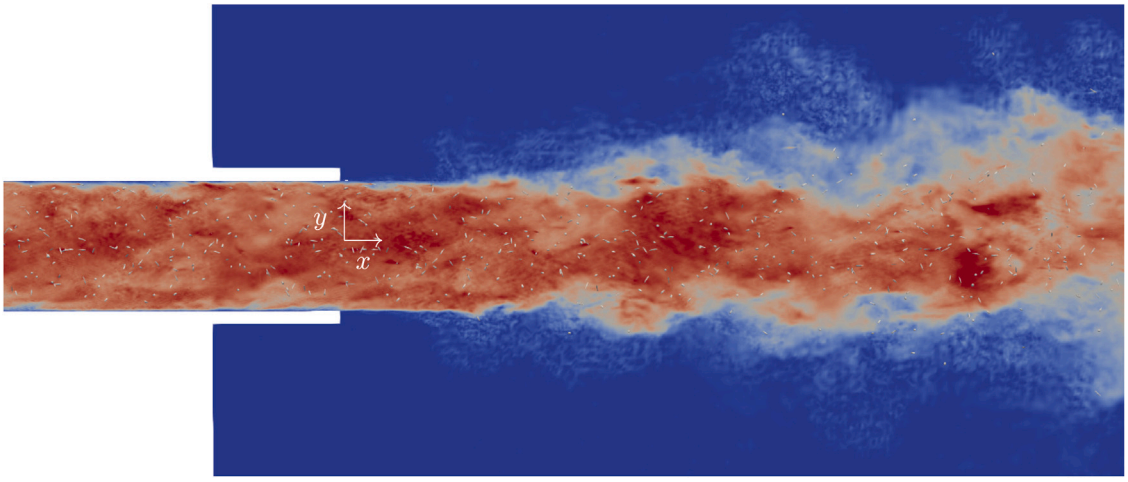

Fig. 10. Instantaneous absolute velocity contours for the particle–laden pipe and jet flow. Particles are shown in gray color.

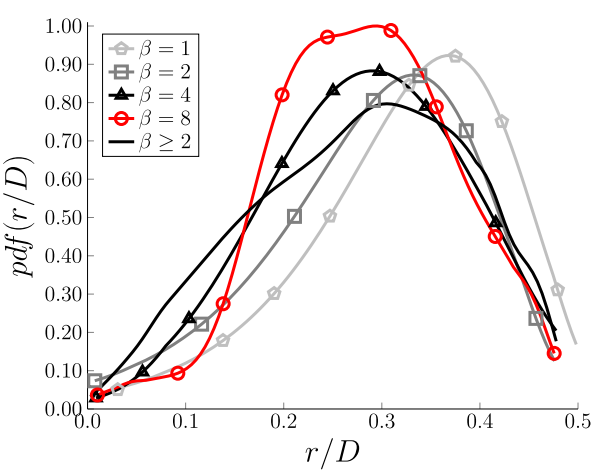

(a) Probability density function normalized to unity of particles with aspect ratio $\beta = 1$, $\beta = 2$, $\beta = 4$, and $\beta = 8$.

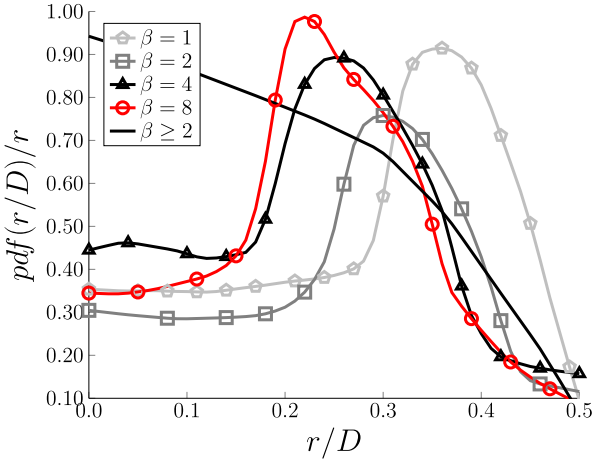

(b) Probability density function normalized to unity of particles with aspect ratio $\beta = 1$, $\beta = 2$, $\beta = 4$, and $\beta = 8$. The results are scaled by $1/r$ to account for the changing cross-sectional area of the radial distances.

Fig. 11. Probability density function normalized to unity of particles with aspect ratio $\beta = 1$, $\beta = 2$, $\beta = 4$, and $\beta = 8$. The solid black line, which represents the mean distribution of the ellipsoidal particles $\beta \geq 2$, shows a preferential distribution in the pipe domain at approx. $r/D \approx 0.32$.

distributions in Fig. 11. The higher radial velocities near the pipe wall for higher aspect ratios indicate larger displacement off the wall.

Several phenomena are identified for the different dynamics of spherical and ellipsoidal particles. Due to the elongated shape, the ratio of the length of prolate particles in relation to the turbulent scales becomes larger than that of spherical particles. Therefore, the ellipsoidal particles experience larger differences in the inhomogeneous turbulent velocity field in the near-wall region. As a result, they are more likely to experience torque, which induces a rotation of the particle. The interaction of the rotating particle with the flow field eventually causes the particle to translate.

In addition, the turbulent velocity profile strengthens the motion of the particles within the domain through the localized loads on the particle surfaces. The spatially varying forces on the particle surfaces are induced by the local eddies such that additional torque and radial momentum are imposed on the surfaces of the particles. The high Stokes number $St_0 = 50$ means that the particles largely maintain their momentum. However, eventually the mechanical loads generated by the large-scale coherent structures in the flow field, i.e., the vertical structures are greater than the particle sizes, impact the particle trajectories. The relative mass distribution within the particles further influences this dynamic as the forces required to induce rotation are lower than those necessary to modulate the linear velocity.

In the following, a more detailed analysis of the impact of the particle aspect ratio β is conducted. The separate particle distributions for $\beta = 2$, $\beta = 4$, and $\beta = 8$ are shown in Fig. 11(a). The particle concentrations show the maximum values to shift towards the pipe center with increasing aspect ratio. The distributions of spherical and prolate ellipsoidal particles with aspect ratio $\beta = 2$ exhibit a close resemblance. In contrast, the ellipsoidal shapes $\beta = 2$ and $\beta = 8$ possess distinctly different distributions. The distribution of the intermediate aspect ratio of $\beta = 4$ lies between the two extremes. For increasing aspect ratio β, the maximum develops a plateau-like distribution which shifts progressively towards the center of the pipe. This behavior can be attributed to enhanced rotational dynamics among elongated particles as discussed before. This results in a more uniform distribution compared to that of spherical particles. Similar phenomena have been reported by Gupta et al. (2018).

It is evident that the particle aspect ratio plays a crucial role in the radial particle distribution. The shift in distribution correlates to localized low radial velocity and increased rotational dynamics.

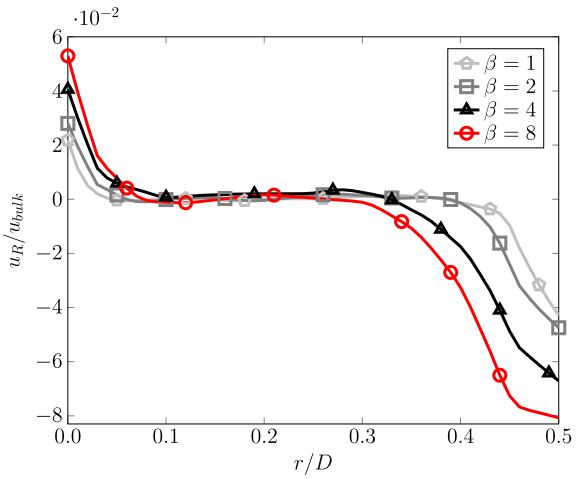

Fig. 12. Signed radial velocity u_R/u_b as a function of the radial position r/D. The preferential concentration by the particles over $0.1 \leq r/D \leq 0.32$ is caused by the lower radial velocity between the pipe center and the wall.

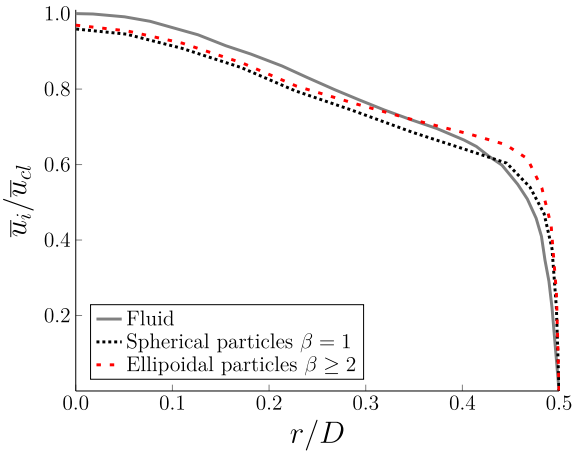

Fig. 13. Fluid velocity $\overline{u}$ and velocities of spherical $\overline{u}_{p,s}$, and ellipsoidal $\overline{u}_{p,e}$ particles as a function of r/D. Near the centerline the particle velocities are smaller than the fluid velocity, while near the pipe wall the opposite is observed. On average, ellipsoidal particles are slightly faster than spherical particles due to the increased surface area exposed to the carrier flow.

6.1.2. Linear velocity statistics

Previous research for spherical particles has shown that the ratio of the particle velocity and the local fluid velocity is a function of the radial position within turbulent pipe flow (Soo and Regalbuto, 1960; Popper et al., 1974).

To investigate this hypothesis for prolates, the time-averaged fluid velocity $\overline{u}$ and the time-averaged particle velocities $\overline{u}_p$ in the streamwise direction are shown in Fig. 13. The velocities for spherical particles are indicated by the subscript $(\cdot)_{p,s}$ and ellipsoidal particles are marked by the subscript $(\cdot)_{p,e}$.

The distributions of the particle velocities $\overline{u}_p$ normalized by the centerline velocity $\overline{u}_{cl}$ in the pipe show that the particle velocity is higher than the local fluid velocity near the pipe wall. The opposite is observed near the centerline.

Kaftori et al. (1995b) reported similar behavior for spherical particles. The authors concluded that the combination of rotational spin and linear movement resulted in increased particle velocities in relation to the local fluid (Kaftori et al., 1995a,b; Mortensen et al., 2008).

A comparison of the relative velocity distribution of the spherical particles and the ellipsoidal particles shows that the overall trend is very similar. The tendency of the particles to have a lower velocity than the fluid flow near the centerline is consistent with the behavior of spherical particles. The same is true near the pipe wall. Due to the equal mass of all particles irrespective of their aspect ratio, the particles have the same Stokes number St_0 and thus, show similar inertial behavior. Hence, the differences are mainly due to the particle shape. The ellipsoidal particles expose a larger surface area to the carrier fluid. Consequently, the ellipsoidal particles tend to experience larger mechanical loads on the windward side and maintain their inertia for a longer time. As a result, the velocity of the ellipsoidal particles near the pipe wall is greater than the spherical particle velocity.

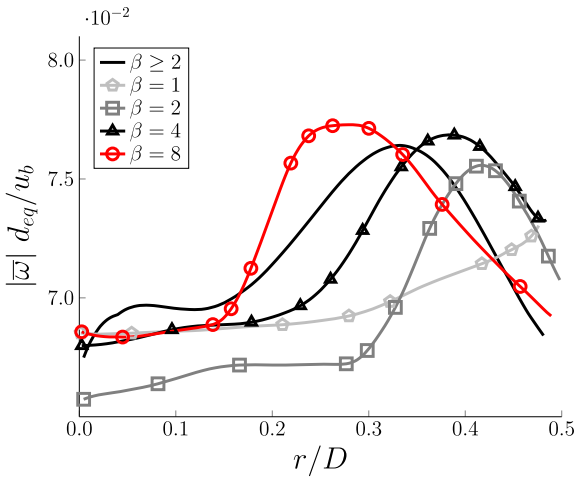

Fig. 14. Mean absolute angular velocity $|\overline{\omega}|\ d_{eq}/u_b$ as a function of r/D. The maximum angular velocity is observed at $r/D \approx 0.32$ which aligns well with the position where the particle velocities are aligned with the fluid velocity, i.e., small differences of the local fluid velocity yield the rotational dynamics.

6.1.3. Rotational statistics

The anisotropic shape of the ellipsoidal particles and the locally varying forces on the particle surface generate rotational forces which are less important for spherical particles. For ellipsoidal particles, this force distribution leads to rotational dynamics and eventually to linear movement due to interaction with the turbulent carrier fluid.

To support this hypothesis, Fig. 14 shows the time-averaged absolute angular velocity $|\overline{\omega}|\ d_{eq}/u_b$ over r/D. The averaged vorticity rates peak at $r/D \approx 0.32$ for $\beta \geq 2$. This is in the range of the radial position where the ratio of the particle to the fluid velocity changes as shown in Fig. 13. The relative velocity at the particle tips of the ellipsoids is more likely of varying direction such that modulations on the surface have a comparably greater impact. This results in increased rotational dynamics due to the locally varying forces and velocities of the fluid.

The enhanced dynamics at $r/D \approx 0.32$ leads to a preferential orientation on average. The relative orientation of the ellipsoidal particles in relation to the streamwise axis is analyzed by the probability distribution function $pdf(\phi_x)$ illustrated in Fig. 15. Considering the illustration in Fig. 2, ϕ_x is the angle between the elongated particle major axis c and the fluid streamwise axis x. The results of the ellipsoidal particles indicate a preferential orientation of approx. 90°. Furthermore, two distinct peaks at $\phi_x = 55°$ and $\phi_x = 125°$, i.e., at approx. ±35° from the mean orientation of 90° are observed. The shear flow and the boundary layer on the pipe walls determine the loads on the particles. An inclination of the ellipsoidal particles of $90° \pm \sim 35°$ results from the pressure and velocity differences at the particle tips. Moreover, note the slight trend towards higher angles for increased aspect ratios.

This finding is in agreement with the results by van Wachem et al. (2015) who reported an average value of approx. 60° – 70° for $\beta =$

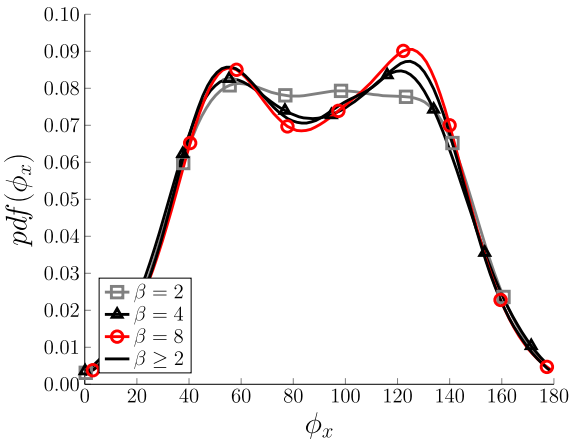

Fig. 15. Probability density function of the particle inclination angle $pdf(\phi_x)$. Except for $\beta = 2$, two peaks are observed at $\phi_x = 55°$ and $\phi_x = 125°$, i.e., a deviation of $\pm 35°$ from the perpendicular orientation.

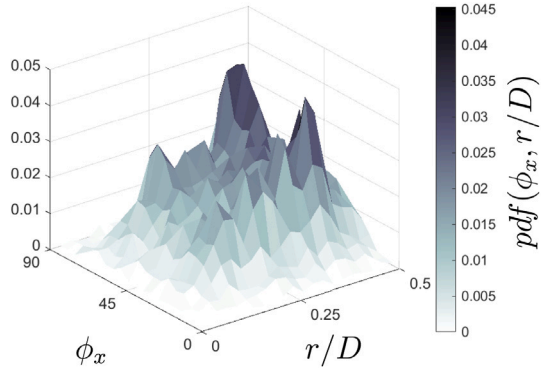

Fig. 16. Multidimensional plot of the probability density function $pdf(r/D, \phi_x)$ for $\beta \geq 2$ as a function of the angle ϕ_x and the radial position r/D. The maxima at $\phi_x = 55°$ and $\phi_x = 125°$ primarily occur near the pipe wall.

2.5 for turbulent channel flow at $Re_\tau = 600$ when wall effects were incorporated.

The probability density function $pdf(r/D, \phi_x)$ as a function of the particle position r/D and the orientation ϕ_x in Fig. 16 evidences that the maxima at $\phi_x = 55°$ and $\phi_x = 125°$ primarily occur near the pipe wall where the ratio of the particle to the fluid velocity changes from > 1 to < 1 (see Fig. 13). Outside of these areas, the distribution is more random and uniform.

The bias towards orientations of $\phi_x = 55°$ and $\phi_x = 125°$ against the streamwise direction near the pipe wall shown in Figs. 15 and 16 strengthens the hypothesis of the strong impact of the local velocity gradient on the particle surfaces of the anisotropic particle geometries.

6.1.4. Multiphase energy exchange

Previous publications have shown a close relationship between the relative velocity ratio of the particle and the local fluid u_p/u and the energy exchange rates in multiphase setups (Vreman, 2007; Zhao et al., 2013). Furthermore, Zhao et al. (2013) have shown that the energy exchange between the two phases due to the mean motion exceeds the exchange caused by the velocity fluctuations. To be more precise, the majority of the energy exchange is associated with the streamwise motions.

In Section 6.1.3 it was shown that the anisotropic ellipsoidal particles undergo additional rotation. It is stated in many publications such as (Tsuji et al., 1984; Vreman, 2007; Cannon et al., 2024; Ljus et al., 2002; Rani et al., 2004; Zhao et al., 2013; Balachandar and Eaton, 2010; Pirozzoli et al., 2021) that this additional rotation impacts the energy exchange. This is investigated in the following.

As shown in the last section, the velocity ratio $\overline{u}_p/\overline{u}$ differs with the relative position of the particles inside the pipe. This results in varying shear-stress and strain rates across the pipe diameter and altered fluid dissipation rates. The ellipsoidal particle shape additionally leads to a more complex dynamics in the particle wake due to entrainment, which further modulates the energy exchange.

The dependence of the particle–fluid energy exchange on $\overline{u}_p/\overline{u}$ is investigated for spherical and ellipsoidal particles. Fig. 17(a) shows the time-averaged energy transfer $\overline{\psi}(r)/(\rho u_0^3/d_{eq})$ between the fluid and the particles as a function of r/D. The convention of $\psi \geq 0$ implies that energy is transferred from the particle to the fluid.

The energy transfer depends on the relative position inside the pipe. It is positive in the near-wall region and negative near the pipe center, i.e., energy is transferred from the particles to the fluid in the near-wall region for all aspect ratios. The particle transfer of energy is predominantly found near the pipe wall where the particle velocity is higher than the fluid velocity $u_p/u > 1$. This emphasizes the strong impact of the ratio of relative velocities and is attributed to the Stokes number St_0.

Since the ellipsoidal particles are on average faster than the spherical particles near the wall, increased energy transfer rates are observed for ellipsoidal particles. Furthermore, larger aspect ratios yield higher transfer rates. Since all particles have the same mass, the surplus in energy transfer is caused by the differences in the relative velocities and the anisotropic shape and the elongated axis which results in rotational dynamics which yields higher energy transfer rates. However, on average the energy due to the rotation is one order of magnitude smaller than the energy transferred by linear movement.

In contrast, the energy exchange near the pipe center is negative, i.e., energy is absorbed by the particles from the fluid. The ratio u_p/u is < 1 which facilitates the transfer of kinetic energy from the fluid to the particles. Since u_p/u is similar for different particle aspect ratios, comparable energy exchange rates are determined.

The particles additionally modulate the fluid dissipation due to the crossing-trajectory effect (Schneiders et al., 2017, 2019). With increasing $\overline{u}_p/\overline{u}$, the modulation is enhanced due to the increased shear stress on the particle surfaces. Additionally, the wake of the particles invokes fluid entrainment and thus, increased dissipation.

Fig. 17(b) shows by the local dissipation rate $\overline{\epsilon}(r)/(\rho u_0^3/d_{eq})$ over r/D that this assumption holds true for spherical and ellipsoidal particles. Qualitatively, the dissipation distribution behaves similar as the interphase energy transfer. The dissipation caused by the ellipsoidal particles is larger than for the spherical shape. This is especially true near the pipe wall where $\overline{u}_p/\overline{u} > 1$, which results in larger relative velocities and thus dissipation rates. Furthermore, the particle tips of the ellipsoids generate localized pressure minima and steep velocity gradients which enhance the dissipation in the flow field.

In summary, the additional dissipation induced by ellipsoidal particles is greater than the energy transferred from the particle to the fluid. Near the pipe wall, energy is transferred towards the fluid and the fluid dissipation is significantly enhanced. Near the centerline, the energy transfer is negative and lower dissipation rates are observed. This is similar for spherical particles. However, a larger particle aspect ratio results in higher additional strain and dissipation.

6.2. Particle–laden turbulent free jet flow

The dynamics and the impact of the particles on the turbulent free jet flow are investigated next. The focus is on the near field $x/D \leq 10$. The spatial dynamics of the particles are presented and their impact on the flow structure are analyzed. Kinetic energy and turbulent intensity statistics are discussed.

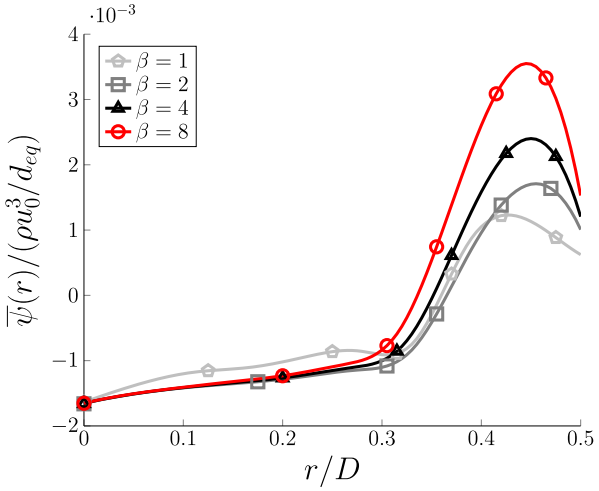

(a) Mean interphase energy exchange $\overline{\psi}(r)$ normalized by $(\rho u_0^3/D)$ showing an increasingly larger energy transfer rate for increasing particle aspect ratio beyond $r/D \geq 0.3$.

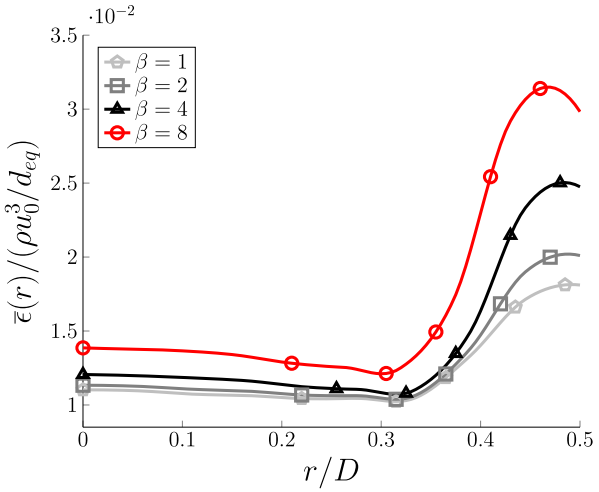

(b) Mean viscous dissipation rate $\overline{\epsilon}(r)$ normalized by $(\rho u_0^3/D)$. The trend of the dissipation rate is similar to that observed in the interphase energy transfer for the various particle aspect ratios.

Fig. 17. Comparison of the mean interphase energy exchange rate $\overline{\psi}$ (a) and the mean viscous dissipation rate $\overline{\epsilon}$ (b) for the investigated particle aspect ratios.

6.2.1. Particle statistics

The near field of the turbulent free jet single-phase flow is characterized by the rapid development of the turbulent scales as described by Ball et al. and Ball et al. (2012), Burattini et al. (2004). Ball et al. summarize that the initial instability modes trigger the development of the flow structures in the shear layer. The subsequent mixing results in vortices which roll-up and stretch the vortices in the potential core (Ball et al., 2012).

According to Ball et al. the development of the flow field in the intermediate region $10 \leq x/D \leq 70$ is characterized by the highly anisotropic turbulent structures formed in the initial phase of the jet interacting with each other before reaching self-similarity in the far field $x/D \geq 70$ (Ball et al., 2012).

The particles impact the flow development due to the particle–fluid energy exchange and local interphase and dissipation modulations as a function of the local position. In the following, the particle linear and rotational dynamics are discussed. Statistics equivalent to the analysis for the pipe flow evidence the impact of the different particle shapes on the turbulent free jet flow.

The probability density distribution $pdf(r/D)$ of the particle positions of different shapes as a function of the radial position r/D at $x/D = 10$, i.e., at the end of the near field, is shown in Fig. 18. The overall shape of the particle distributions is quite similar for the different particle aspect ratios.

However, the ellipsoidal particles show a slightly wider radial distribution in comparison to spherical particles and the spreading increases for larger β.

When investigating the maximum of the probability density function, ellipsoidal particles of larger aspect ratios tend to align further away from the jet centerline.

The location of the maximum of the probability density function $r_{max,x/D}$ is plotted in the streamwise direction x/D in Fig. 19(a) normalized by the location at the jet exit $r_{max,0}$. It is evident that ellipsoidal particles spread faster in radial direction than spherical particles. While the maximum of the PDF for spherical particles $\beta = 1$ changes its location only marginally, ellipsoids with an aspect ratio $\beta = 8$ show a three times higher spreading compared to $\beta = 1$.

The standard deviation $SD = \sqrt{\frac{1}{N-1}\sum_{i=0}^{N} |pdf(r/D) - \psi_{mean}|_i^2}$ with the mean of the distribution ψ_{mean} at the respective distance x/D is shown in Fig. 19(b) for the different aspect ratios. The deviation from

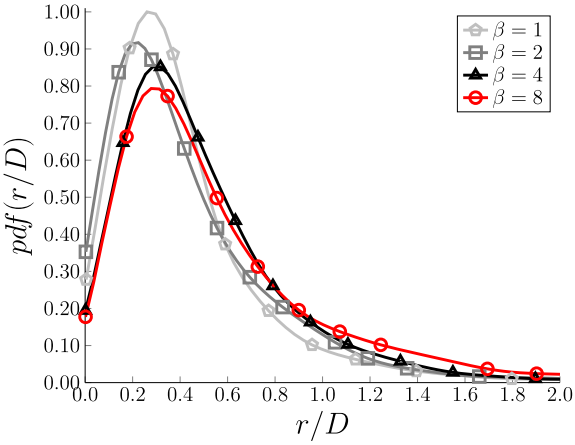

Fig. 18. Probability density function normalized to unity of particles with aspect ratio $\beta = 1$, $\beta = 2$, $\beta = 4$, and $\beta = 8$ at $x/D = 10$ in turbulent free jet flow. The particles show similar distributions for all investigated aspect ratios, which indicates that the impact of the aspect ratio gradually diminishes in free jet flow.

the mean increases for all aspect ratios in the streamwise direction x/D until $x/D \approx 3$. Further downstream, the standard deviation decreases which implies that particles tend to cluster closer together with increasing distances from the nozzle exit. It can be concluded that the aspect ratio of the particles has a large impact on their spreading rate in the turbulent free jet.

The higher spreading of the ellipsoidal particles in the turbulent free jet flow is correlated to their increased rotational dynamics.

The probability density function $pdf(|\overline{\omega}|\ d_{eq}/u_b)$ of the absolute angular velocity $|\overline{\omega}|\ d_{eq}/u_b$ is shown at $x/D = 5$ and $x/D = 10$ in Fig. 20. The distributions show that ellipsoidal particles with an aspect ratio of $\beta = 8$ possess higher angular velocities compared to particles with smaller aspect ratios. Further downstream at $x/D = 10$, the angular velocity slightly increases for all aspect ratios in comparison to $x/D = 5$.

Since the jet free-shear layer merges towards the end of the potential core the particles are subject to larger scale fluctuations in the turbulent

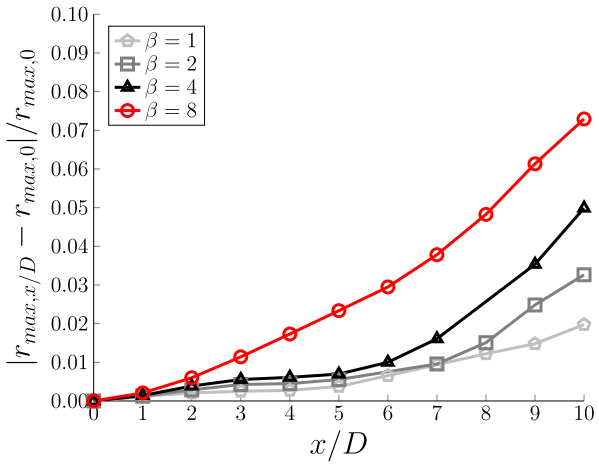

(a) Spreading of the location of the maximum of the PDF $r_{max,x/D}$ normalized by its initial location $r_{max,0}$ showing an increasing spreading with increasing aspect ratio.

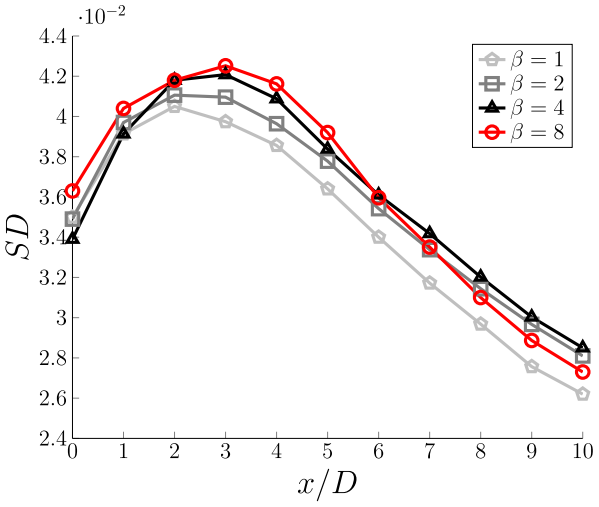

(b) Standard deviation SD of the mean distributions as a function of the streamwise coordinate x/D.

Fig. 19. Particle spreading in turbulent free jet flow. The particle aspect ratios cause different lateral spreading rates in the streamwise direction x/D.

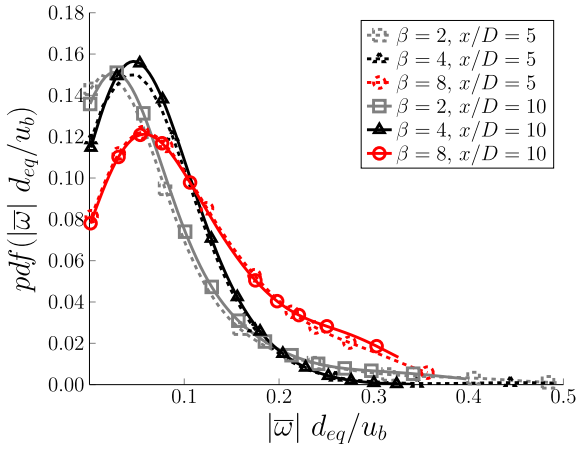

Fig. 20. Probability density function $pdf(|\overline{\omega}|\ d_{eq}/u_b)$ of the absolute angular velocity $|\overline{\omega}|\ d_{eq}/u_b$ for $x/D = 5$ (dashed) and $x/D = 10$ (solid).

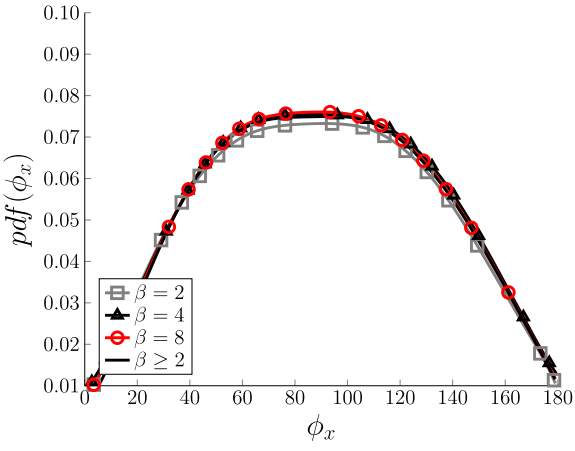

Fig. 21. Probability density function $pdf(\phi_x)$ of the particle orientation ϕ_x at $x/D = 10$ for ellipsoidal particles.

jet, which increases the likelihood of varying surface forces around the particles such that the rotational dynamics is enhanced.

Fig. 21 shows the average orientation of all ellipsoidal particles $\beta \geq 2$ and the individual orientation of the $\beta = 2$, $\beta = 4$, and $\beta = 8$ at the end of the near field $x/D = 10$. The alignment with the streamwise axis is similar to the result in Fig. 15 for the pipe flow. However, the dip at $\phi_x \approx 90°$ has disappeared.

In other words, the particles tend to align normal to the streamwise direction without any clear deviations. Compared to the pipe flow, the velocity gradients in the radial direction are reduced such that the forces on the particle surface are more evenly distributed. The ellipsoidal particles consequently tend to behave as bluff bodies. Similar results are reported by Fröhlich et al. (2021) who investigated settling ellipsoids in isotropic decaying turbulence by means of Lagrangian point-particle models.

6.2.2. Jet structure

The flow structure of a free jet is characterized by the development of the free-shear layer and the potential core. The velocity profile in Fig. 22 shows the single and multiphase solution in the potential core at $x/D = 1$. The single-phase jet velocity profile is wider than that of the particle–laden jet whose radial extension is reduced by approx. 4%. The narrower extension is compensated by a slightly higher peak velocity on the centerline. Due to the small distance to the jet exit plane, it is clear that the distributions in Fig. 22 are strongly affected by the upstream pipe flow.

The particle–laden potential core has a higher mean velocity on its centerline. Due to the relative transfer of kinetic energy inside the potential core resulting from the spatially varying ratio of interphase energy exchange and increased dissipation rates, the shear layer of the jet is modulated. This means that the kinetic energy is more centralized to the core compared to the single-phase case. This results in lower velocity gradients in the radial direction which further impacts the energy decay rates. As a consequence of the altered core geometry, the length of the potential core is significantly increased. The length is defined by the position where the centerline velocity is less than 90% of its initial value, i.e., $x_{cl}(\overline{u}_{cl}/\overline{u}_{cl,0} = 0.9)$.

To counterbalance the elevated velocities on the centerline, Fig. 23 shows that the distribution of the centerline velocity of the particle–laden flow has a steeper decrease. The dynamics of the turbulent free jet flow in the near field ($0 \leq x/D \leq 10$) evolve similarly to a sudden expansion. Due to the free-shear layers, turbulence further develops before reaching self-similarity further downstream.

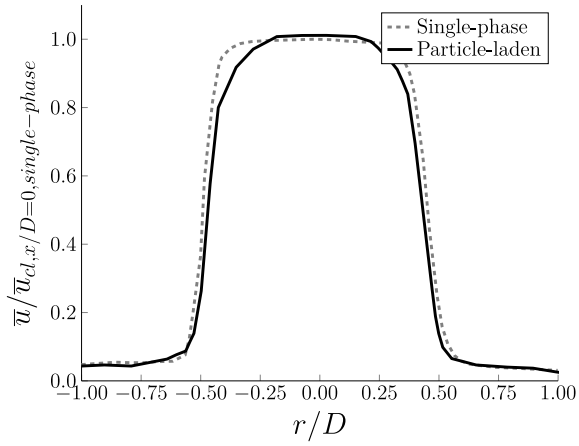

Fig. 22. Radial extension of the velocity $\overline{u}/\overline{u}_{cl,x/D=0,single-phase}$ for the single-phase and particle–laden case at $x/D = 1$. The radial extension of the velocity is reduced by 4% for the particle–laden jet yielding a higher maximum velocity on the centerline.

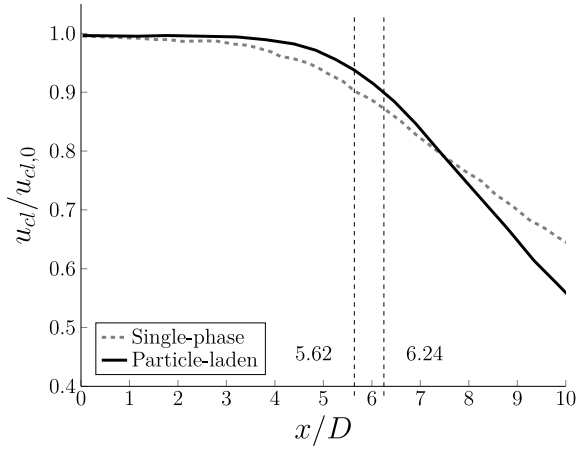

Fig. 23. Development of the velocity $\overline{u}_{cl}/\overline{u}_{cl,0}$ in the streamwise direction for the single-phase and the particle–laden flow. The location at which the velocity drops below 90% of its initial value is moved downstream from $x/D = 5.62$ to $x/D = 6.24$ in the particle–laden case, i.e., by $\sim 10\%$.

Hence, Fig. 23 shows that the decay of fluid energy is greater at $x/D \geq 7$ for the particle–laden jet flow. The previously outlined tendency of the particles to increase the local fluid dissipation is related to the inertia forces of the particles. To be more precise, the inertia of the particles in the turbulent free jet decreases due to the spreading of the jet. Consequently, the fluid velocity is higher than the particle velocity which lowers the fluid kinetic energy. The tendency to break up coherent turbulent structures and enhance the transfer from the large-scale to the small-scale motions in the near field is well known (Burattini et al., 2004; Ball et al., 2012). This is further intensified by the particles which facilitate the break-up process. This statement is further investigated in the following.

6.2.3. Fluid kinetic energy

The temporal development of the total kinetic energy of the fluid in the near field is shown in Fig. 24 for the single-phase jet and the particle–laden jet normalized by the maximum kinetic energy $E_{k,max,single-phase}$ of the single-phase flow. The kinetic energy is integrated in a volume $[0 \leq x/D \leq 10, -5 \leq y \leq 5, -5 \leq z \leq 5]$ and is normalized by the kinetic energy of the single-phase flow and the integrated volume, i.e., excluding the volume of the embedded

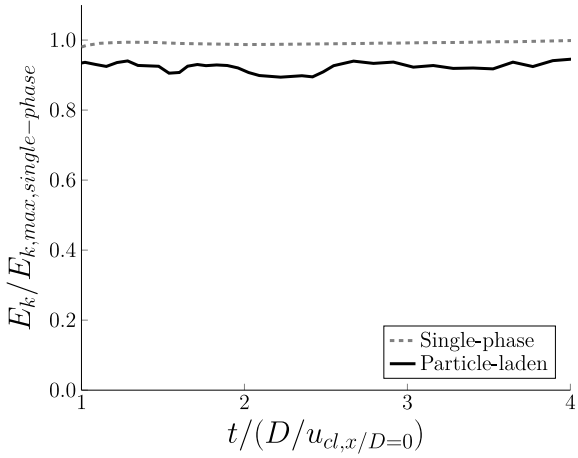

Fig. 24. Temporal development of the normalized fluid kinetic energy of the single-phase and particle–laden flow. In comparison to the single-phase turbulent free jet, the particle–laden jet is reduced by 9.1% on average and small-scale fluctuations are present.

particles. The distribution of the single-phase jet possesses hardly any fluctuations. The kinetic energy reaches an almost steady value. The particle–laden jet fluctuates, it shows an unsteady distribution caused by the energy modulations of the carrier flow imposed by the particles. The fluid kinetic energy in the particle–laden jet is reduced by approx. 9.1%. The kinetic energy distribution does not converge to a constant steady state value since the number of particles and their aspect ratios vary temporally in the jet volume.

6.2.4. Fluid turbulence intensity

The impact of different particle shapes on the turbulence intensity in fluid flow depends on various parameters (Gore and Crowe, 1989; Tsuji et al., 1984; Vreman, 2007; Sheen et al., 1994; Ljus et al., 2002).

To assess the impact of non-spherical, ellipsoidal particles on the intensity of the turbulent scales, the turbulence intensity $\sqrt{\overline{u'^2}}/U_m$ normalized by the single-phase maximum turbulence intensity is evaluated along the centerline. It is shown in Fig. 25 for the single-phase and the particle–laden jet. Overall, the distributions follow a similar trend. Initially, the development of the turbulence intensity is identical. At the nozzle exit, the initial instabilities generated by the free-shear layer result in turbulent flow structures which convect downstream (Burattini et al., 2004; Ball et al., 2012). Vortex roll-ups occur which enhance the spreading of the jet in the near field. This interaction breaks up coherent structures resulting in the development of the turbulent fluctuations in the later stages of the jet development (Ball et al., 2012; Burattini et al., 2004). The tendency is enforced by the particles which are known to break up coherent large-scale motions (Feng et al., 2024). The turbulence intensity of the particle–laden jet and the single-phase jet diverge at $x/D \geq 3$ where the particle–laden jet is severely damped.

The increased break-up of coherent structures and the higher dissipation due to the velocity differences between the carrier fluid and the particles cause the energy of the fluid to decrease and the turbulence intensity to be weakened. As shown before, the dissipation rate is impacted by the anisotropic particle shapes and the rotational dynamics. Therefore, the dissipation of the fluid is increased by the increased stress on the particle surfaces resulting in the steep drop off shown in Fig. 23. At the end of the near field, the turbulence intensity is reduced by approx. 20%.

7. Conclusion

The impact of spherical and ellipsoidal particles on the overall flow structure in turbulent free jet flow is investigated. The particles possess

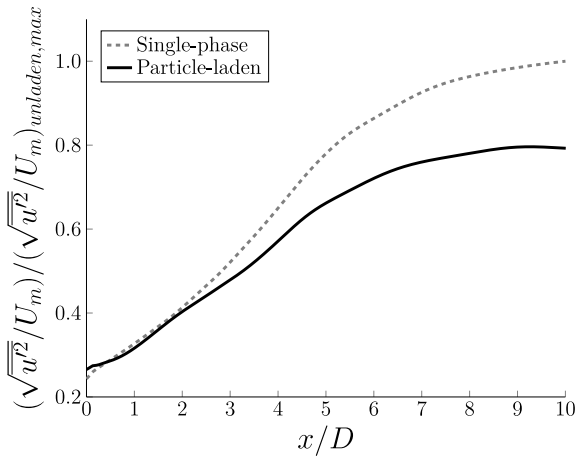

Fig. 25. Streamwise development of the turbulence intensity $\sqrt{\overline{u'^2}}/U_m$ normalized by the single-phase maximum turbulence intensity $(\sqrt{\overline{u'^2}}/U_m)_{max}$ on the centerline for the single-phase and particle–laden jet. The initial development is similar. However, the intensity is strongly damped at $x/D \geq 3$ in the particle–laden jet due to the effect of the particles on the large-scale structures.

aspect ratios in the range $1 \leq \beta \leq 8$. The simulations are performed using a cut-cell method in a finite-volume formulation. The surfaces are described by a level set method. Together with the multi cut-cell method highly accurate results in which mass, momentum, and energy are conserved, were achieved.

The turbulent free jet is computed simultaneous with a pipe flow. The latter provides the inflow data for the jet. This setup ensures physically correct particle and fluid properties at the jet inflow boundary.

The particle dynamics and flow characteristics of the fully-developed periodic pipe flow are investigated separate from the turbulent free jet flow. The particle distribution is assessed and the preferred orientation as a function of the varying particle aspect ratios is outlined. The results show preferential concentrations and orientations based on the particle aspect ratio and the relative position inside the pipe. For increasing aspect ratios, the distribution of the particles inside the pipe takes a more uniform distribution. Whereas spherical particles tend to align close to the pipe wall, ellipsoidal particles tend to align throughout the domain as the aspect ratio β increases. The major reason for the different distribution inside the pipe is the anisotropic particle shape, i.e., the elongated major axis. Due to the particle shape, rotational movement is induced that leads to increased spanwise dynamics. Preferential orientations of the ellipsoidal particles are identified at $\phi_x \approx 55°$ and $\phi_x \approx 125°$, i.e., $90° \pm \sim 35°$ where ϕ_x is the inclination angle against the streamwise direction. The almost perpendicular orientation is caused by the relative velocity and pressure differences at the particle tips of the anisotropic particles resulting in varying mechanical forces at the particle surfaces. The particles interact with the carrier fluid by transferring kinetic energy to and from the fluid. Depending on the relative position inside the pipe, all particles are shown to extract energy from the pipe center and to transfer energy to the fluid towards the pipe walls. This tendency is further amplified by the aspect ratio, i.e., a higher aspect ratio tends to increase the energy transfer. The particles are shown to additionally induce dissipation in the fluid. Similar trends as to the energy transfer are observed although varying in magnitude. The magnitude of the induced dissipation is on average larger than the energy transfer. This is shown to be caused by the additional rotational dynamics of the ellipsoidal particles and the relative velocity differences between the fluid and the particles.

Subsequently, the turbulent free jet flow is analyzed with emphasis on the near field region $x/D \leq 10$. The jet flow is modulated by the particles. That is, the jet radial extension is reduced by approx. 4% due to the particles. The velocity along the centerline has a steeper negative slope in the particle–laden jet since the particles induce additional dissipation. The comparison of the kinetic energy budgets between a single-phase and the particle–laden jet reveals an attenuation of the fluid kinetic energy by approx. 9% through the particles. The turbulence intensity is reduced by approx. 20%.

In the future, a turbulent non-isothermal free jet will be analyzed, i.e., the impact of varying temperature between carrier flow and particles due to the locally varying heat transfer will be investigated.

Additionally, shape and mass changes will be investigated since solid particles undergo significant shape and mass changes during combustion processes (Riaza et al., 2020; Holmgren et al., 2017). In the present work, it was shown that the different shapes of the particles lead to varying concentrations and modulations of the carrier flow. Hence, the temporally changing aspect ratio of the particles likely will lead to different results.

Furthermore, mass changes result in varying Stokes numbers and as such in varying inertial dynamics. It is expected to observe larger radial dynamics of the particles due to smaller inertia at lower Stokes numbers. The particles are most likely to closer follow the turbulent eddies and the energy exchange is expected to be weakened. Consequently, the fluid kinetic energy would be modulated by a lesser degree and the statistics will be closer to the single-phase flow configuration. For larger Stokes numbers, the opposite is expected.

CRediT authorship contribution statement

Thede Kiwitt: Writing – original draft, Visualization, Validation, Software, Methodology, Investigation, Formal analysis, Data curation, Conceptualization. **Matthias Meinke:** Writing – review & editing, Supervision, Resources, Project administration, Funding acquisition. **Dominik Krug:** Writing – review & editing, Supervision. **Wolfgang Schröder:** Writing – review & editing, Supervision, Resources, Project administration, Funding acquisition.

Declaration of competing interest

The authors declare that they have no known competing financial interests or personal relationships that could have appeared to influence the work reported in this paper.

Acknowledgments

This work has been funded by the German Research Foundation (DFG) within the project SCHR 309/73-1. The support is gratefully acknowledged. Computing resources were provided by the High Performance Center Stuttgart (HLRS) and by the Jülich Supercomputing Centre (JSC) within a Large-Scale Project of the Gauss Centre for Supercomputing (GCS).

Data availability

Data will be made available on request.

References

Bach, W., 1981. Fossil fuel resources and their impacts on environment and climate. Int. J. Hydrog. Energy 6 (2), 185–201.
Balachandar, S., Eaton, J.K., 2010. Turbulent dispersed multiphase flow. Annu. Rev. Fluid Mech. 42 (1), 111–133.
Ball, C., Fellouah, H., Pollard, A., 2012. The flow field in turbulent round free jets. Prog. Aerosp. Sci. 50, 1–26.
Bec, J., Vallée, R., 2024. Homogeneous turbophoresis of heavy inertial particles in turbulent flow. J. Fluid Mech. 999, A83.
Black, D.L., McQuay, M.Q., 2001. Laser-based particle measurements of spherical and nonspherical particles. Int. J. Multiph. Flow 27 (8), 1333–1362.

Burattini, P., Antonia, R., Rajagopalan, S., Stephens, M., 2004. Effect of initial conditions on the near-field development of a round jet. Exp. Fluids 37, 56–64.
Cannon, I., Olivieri, S., Rosti, M.E., 2024. Spheres and fibers in turbulent flows at various Reynolds numbers. Phys. Rev. Fluids 9 (6), 064301.
Chin, C., Monty, J., Ooi, A., 2014. Reynolds number effects in DNS of pipe flow and comparison with channels and boundary layers. Int. J. Heat Fluid Flow 45, 33–40.
Chin, C., Ooi, A., Marusic, I., Blackburn, H., 2010. The influence of pipe length on turbulence statistics computed from direct numerical simulation data. Phys. Fluids 22 (11).
Crowe, C.T., 2005. Multiphase Flow Handbook. CRC Press.
Dufek, J., Manga, M., Patel, A., 2012. Granular disruption during explosive volcanic eruptions. Nat. Geosci. 5 (8), 561–564.
Feng, Y., Liu, H., Zheng, X., 2024. The modulation of coherent structures by the near-wall motions of particles. J. Fluid Mech. 981, A26.
Fröhlich, K., Farmand, P., Pitsch, H., Meinke, M., Schröder, W., 2021. Particle Reynolds number effects on settling ellipsoids in isotropic turbulence. Int. J. Multiph. Flow 139, 103566.
García, R., Pizarro, C., Lavín, A.G., Bueno, J.L., 2017. Biomass sources for thermal conversion. Techno-economical overview. Fuel 195, 182–189.
Glowinski, R., Pan, T.-W., Hesla, T.I., Joseph, D.D., Periaux, J., 2001. A fictitious domain approach to the direct numerical simulation of incompressible viscous flow past moving rigid bodies: application to particulate flow. J. Comput. Phys. 169 (2), 363–426.
Gore, R., Crowe, C.T., 1989. Effect of particle size on modulating turbulent intensity. Int. J. Multiph. Flow 15 (2), 279–285.
Günther, C., Meinke, M., Schröder, W., 2014. A flexible level-set approach for tracking multiple interacting interfaces in embedded boundary methods. Comput. & Fluids 102, 182–202.
Guo, Q., Chen, X., Liu, H., 2012. Experimental research on shape and size distribution of biomass particle. Fuel 94, 551–555.
Guo, N., Li, T., Zhao, L., Løvås, T., 2019. Eulerian-Lagrangian simulation of pulverized biomass jet using spheroidal particle approximation. Fuel 239, 636–651.
Gupta, A., Clercx, H., Toschi, F., 2018. Effect of particle shape on fluid statistics and particle dynamics in turbulent pipe flow. Eur. Phys. J. E 41, 1–15.
Hartmann, D., Meinke, M., Schröder, W., 2008. An adaptive multilevel multigrid formulation for cartesian hierarchical grid methods. Comput. & Fluids 37 (9), 1103–1125.
Holmgren, P., Wagner, D.R., Strandberg, A., Molinder, R., Wiinikka, H., Umeki, K., Broström, M., 2017. Size, shape, and density changes of biomass particles during rapid devolatilization. Fuel 206, 342–351.
Hutter, K., 2005. Geophysical granular and particle-laden flows: review of the field. Philos. Trans. R. Soc. A: Math. Phys. Eng. Sci. 363 (1832), 1497–1505.
Kaftori, D., Hetsroni, G., Banerjee, S., 1995a. Particle behavior in the turbulent boundary layer. I. Motion, deposition, and entrainment. Phys. Fluids 7 (5), 1095–1106.
Kaftori, D., Hetsroni, G., Banerjee, S., 1995b. Particle behavior in the turbulent boundary layer. II. Velocity and distribution profiles. Phys. Fluids 7 (5), 1107–1121.
Kim, H.-K., Ahn, B., 2021. Effect of al2o3 sandblasting particle size on the surface topography and residual compressive stresses of three different dental zirconia grades. Materials 14 (3), 610.
Lau, T.C., Nathan, G.J., 2014. Influence of Stokes number on the velocity and concentration distributions in particle-laden jets. J. Fluid Mech. 757, 432–457.
Ljus, C., Johansson, B., Almstedt, A.-E., 2002. Turbulence modification by particles in a horizontal pipe flow. Int. J. Multiph. Flow 28 (7), 1075–1090.
Martins, F., Felgueiras, C., Smitkova, M., Caetano, N., 2019. Analysis of fossil fuel energy consumption and environmental impacts in European countries. Energies 12 (6), 964.
McElroy, M., Carr, R., Ensor, D., Markowski, G., 1982. Size distribution of fine particles from coal combustion. Science 215 (4528), 13–19.
McKendry, P., 2002. Energy production from biomass (part 1): overview of biomass. Bioresour. Technol. 83 (1), 37–46.
Mortensen, P., Andersson, H., Gillissen, J., Boersma, B., 2008. Dynamics of prolate ellipsoidal particles in a turbulent channel flow. Phys. Fluids 20 (9).
Mylläri, F., Karjalainen, P., Taipale, R., Aalto, P., Häyrinen, A., Rautiainen, J., Pirjola, L., Hillamo, R., Keskinen, J., Rönkkö, T., 2017. Physical and chemical characteristics of flue-gas particles in a large pulverized fuel-fired power plant boiler during co-combustion of coal and wood pellets. Combust. Flame 176, 554–566.
Niemöller, A., Schlottke-Lakemper, M., Meinke, M., Schröder, W., 2020. Dynamic load balancing for direct-coupled multiphysics simulations. Comput. & Fluids 199, 104437.
Papadopoulos, G., Pitts, W.M., 1999. A Generic Centerline Velocity Decay Curve for Initially Turbulent Axisymmetric Jets. J. Fluids Eng. 121 (1), 80–85.
Pirozzoli, S., Romero, J., Fatica, M., Verzicco, R., Orlandi, P., 2021. One-point statistics for turbulent pipe flow up to $Re_\tau \approx 6000$. J. Fluid Mech. 926, A28.
Popper, J., Abuaf, N., Hetsroni, G., 1974. Velocity measurements in a two-phase turbulent jet. Int. J. Multiph. Flow 1 (5), 715–726.
Qi, G., Nathan, G.J., Lau, T.C., 2015. Velocity and orientation distributions of fibrous particles in the near-field of a turbulent jet. Powder Technol. 276, 10–17.
Rani, S.L., Winkler, C., Vanka, S., 2004. Numerical simulations of turbulence modulation by dense particles in a fully developed pipe flow. Powder Technol. 141 (1–2), 80–99.
Reeks, M., 1983. The transport of discrete particles in inhomogeneous turbulence. J. Aerosol Sci. 14 (6), 729–739.
Riaza, J., Mason, P.E., Jones, J.M., Williams, A., Gibbins, J., Chalmers, H., 2020. Shape and size transformations of biomass particles during combustion. Fuel 261, 116334.
Schneiders, L., Fröhlich, K., Meinke, M., Schröder, W., 2019. The decay of isotropic turbulence carrying non-spherical finite-size particles. J. Fluid Mech. 875, 520–542.
Schneiders, L., Günther, C., Meinke, M., Schröder, W., 2016. An efficient conservative cut-cell method for rigid bodies interacting with viscous compressible flows. J. Comput. Phys. 311, 62–86.
Schneiders, L., Hartmann, D., Meinke, M., Schröder, W., 2013. An accurate moving boundary formulation in cut-cell methods. J. Comput. Phys. 235, 786–809.
Schneiders, L., Meinke, M., Schröder, W., 2017. Direct particle–fluid simulation of Kolmogorov-length-scale size particles in decaying isotropic turbulence. J. Fluid Mech. 819, 188–227.
Sheen, H., Jou, B., Lee, Y., 1994. Effect of particle size on a two-phase turbulent jet. Exp. Therm. Fluid Sci. 8 (4), 315–327.
Siewert, C., Kunnen, R., Meinke, M., Schröder, W., 2014. Orientation statistics and settling velocity of ellipsoids in decaying turbulence. Atmos. Res. 142, 45–56.
Soo, S., Regalbuto, J., 1960. Concentration distribution in two-phase pipe flow. Can. J. Chem. Eng. 38 (5), 160–166.
Tsuji, Y., Morikawa, Y., Shiomi, H., 1984. LDV measurements of an air-solid two-phase flow in a vertical pipe. J. Fluid Mech. 139, 417–434.
Tun, M.M., Juchelkova, D., Win, M.M., Thu, A.M., Puchor, T., 2019. Biomass energy: An overview of biomass sources, energy potential, and management in Southeast Asian countries. Resources 8 (2), 81.
Vreman, A., 2007. Turbulence characteristics of particle-laden pipe flow. J. Fluid Mech. 584, 235–279.
van Wachem, B., Zastawny, M., Zhao, F., Mallouppas, G., 2015. Modelling of gas-solid turbulent channel flow with non-spherical particles with large Stokes numbers. Int. J. Multiph. Flow 68, 80–92.
Wegmann, T., Niemöller, A., Meinke, M., Schröder, W., 2025. Parallel Eulerian-Lagrangian coupling method on hierarchical meshes. J. Comput. Phys. 521, 113509.
White, F.M., 2006. Viscous Fluid Flow, vol. 3, McGraw-Hill New York.
Zhao, L., Andersson, H.I., Gillissen, J.J., 2013. Interphasial energy transfer and particle dissipation in particle-laden wall turbulence. J. Fluid Mech. 715, 32–59.